Ab initio theoretical studies on U^{3+} and on the structure and spectroscopy of U^{3+} substitutional defects in Cs_2NaYCl_6, $5f^26d^1$ manifold

Luis Seijo[a)] and Zoila Barandiarán

Departamento de Química, C-XIV, and Instituto Universitario de Ciencia de Materiales Nicolás Cabrera, Universidad Autónoma de Madrid, 28049 Madrid, Spain

In this paper we present the results of spin–orbit relativistic *ab initio* model potential embedded cluster calculations of the $5f^26d^1$ excited manifold of $(UCl_6)^{3-}$ embedded in a reliable representation of the Cs_2NaYCl_6 elpasolite host. They are aimed at interpreting the $5f^3 \rightarrow 5f^26d^1$ absorption bands reported by Karbowiak *et al.* [J. Chem. Phys. **108**, 10181 (1998).] An excellent agreement is found between the calculated energies of the absorption transitions from the ground state $5f^3\,1\,\Gamma_{8u}(^4I_{9/2})$ and the experimental data, which supports a detailed interpretation of the electronic nature of the absorption spectrum in the energy region 14 000–23 000 cm^{-1}. In particular, the three unidentified electronic origins that had been experimentally detected are now assigned, and the observed bands are interpreted as having multiple electronic origins. From the structural point of view, the excited states of the $5f^26d^1$ manifold are classified in two sets of main configuration $5f^26d(t_{2g})^1$ and $5f^26d(e_g)^1$ with bond distances R$_e$ [$5f^26d(t_{2g})^1$]<R$_e$[$5f^3$] <R$_e$[$5f^26d(e_g)^1$]. The energies of the $5f^26d^1$ manifold of free U^{3+} have also been calculated; experimental data on them are not available in the literature to the best of our knowledge. These results contribute to show that wave function based *ab initio* methods can provide useful structural and spectroscopic information, complementary to the experimental data, in studies on actinide ion impurities doping ionic hosts, where large manifolds of $5d^{n-1}6d^1$ excited states are involved. © *2003 American Institute of Physics.* [DOI: 10.1063/1.1555120]

I. INTRODUCTION

Actinide impurity ions in ionic hosts have large manifolds of excited states of the $5f^{n-1}6d^1$ configuration which are interesting from basic and applied points of view. In the free ions, these states are much higher in energy than those of the $5f^n$ configuration, but the energy required for a $5f \rightarrow 6d$ excitation is very much reduced in crystals and is strongly dependent on the crystal host.[1,2] This excitation energy is lower than the $4f \rightarrow 5d$ excitation in lanthanide ion doped crystals, where $5d \rightarrow 4f$ broad emission bands are involved in applications as phosphors, scintillators, and visible-UV solid-state laser materials.[3–5] The $f^{n-1}d^1$ energy levels of f-element impurity ions may be involved in photon cascade emission processes[6] and act as intermediate states in electronic Raman scattering[7] and in photon upconversion processes.[8,9] Also, the relative low energy of the $5f^{n-1}6d^1$ levels of the actinide impurity ions makes the analysis of the $5f \rightarrow 5f$ spectra more complex.[10] $5f \rightarrow 6d$ absorption and $6d \rightarrow 5f$ emission transitions have been observed in actinide ion impurities (e.g., Pa^{4+}:Cs_2ZrCl_6,[11,12] U^{3+}:Cs_2NaYCl_6,[10] or Cm^{3+}:Cs_2NaYCl_6[13]) but they are often not well understood and detailed assignments have only been made in the $5f^1 \rightarrow 6d^1$ case.[12]

In these circumstances, wave function-based *ab initio* methods of quantum chemistry are indicated, provided that they include all the relevant interactions: all the bonding interactions within the cluster formed by the impurity and its first coordination shell, including electron correlation effects and scalar and spin–orbit coupling relativistic effects, and the embedding interactions between the cluster and the rest of the host. In this line, *ab initio* calculations of the $5f^n$ manifold and of some charge transfer states of actinyl ions have been shown to be instrumental in the understanding of their electronic structure and spectra in solid state and in solution.[14–17] Also, spin–orbit relativistic *ab initio* model potential (AIMP) embedded cluster calculations[18] have been shown to produce reliable results of the small $6d^1$ manifold of Pa^{4+} in Cs_2ZrCl_6, providing a new interpretation of the absorption spectrum,[19] and of the large $5f^16d^1$ manifold of U^{4+} in Cs_2ZrCl_6, suggesting its involvement in the mechanism of green to blue light upconversion.[20]

In this paper, we present the results of AIMP theoretical calculations of the large $5f^26d^1$ manifold of U^{3+} in the Cs_2NaYCl_6 host. They are aimed at interpreting the rich $5f^3 \rightarrow 5f^26d^1$ absorption bands that have been reported by Karbowiak *et al.*[10] and lack a detailed assignment. The results on the same manifold of free U^{3+} ion are also presented; they are an important reference for the interpretation of the levels of the U^{3+} impurities in solid hosts and they are not available in the literature.

II. DETAILS OF THE CALCULATIONS

The interest of this paper is focused on a large manifold of electronic states of U^{3+}-doped Cs_2NaYCl_6 that are localized on the U^{3+} impurities. These impurities substitute for

a)Electronic mail: luis.seijo@uam.es

some of the Y^{3+} ions in an O_h site with a first coordination shell of six Cl^- ions.[10] These local states depend, mainly, on all the electronic interactions within U^{3+} and on the bonding interactions between U^{3+} and the six Cl^- ions, and, to a lesser extent, on the interactions between the $(UCl_6)^{3-}$ cluster and the rest of the host. In consequence, a method is needed which reliably considers: (i) the scalar and spin–orbit coupling relativistic effects of uranium, (ii) a significant amount of electron correlation effects in a large number of states of the $(UCl_6)^{3-}$ cluster, and (iii) the classical and quantum embedding effects brought about by the Cs_2NaYCl_6 ionic host into the $(UCl_6)^{3-}$ cluster. We have used the AIMP embedding method[21] for the third purpose, together with the Wood–Boring[22]-based effective core potential two-component relativistic Hamiltonian WB-AIMP[23] for the first one. The simultaneous treatment of electron correlation and spin–orbit coupling, which is very demanding here, has been handled by means of spin–orbit multireference configuration interaction calculations (MRCI) using the spin-free-state-shifted Hamiltonian,[24] which allows to transfer electron correlation effects from calculations with a spin-free Hamiltonian to calculations with a spin–orbit Hamiltonian. Bonding interactions and nondynamic correlation effects have been taken into account in complete active space self-consistent field calculations, CASSCF,[25] and multistate complete active space second-order perturbation theory, MS-CASPT2,[26–29] has been used in order to handle the additional nondynamic correlation effects in the large number of $(UCl_6)^{3-}$ excited states involved.

A. Embedded cluster Hamiltonian

The AIMP Hamiltonian that corresponds to the previous description of the method is fully detailed in Ref. 18. We summarize it here. It is the following valence only, spin–orbit relativistic Hamiltonian of the $(UCl_6)^{3-}$ cluster embedded in a Cs_2NaYCl_6 lattice:

$$
\begin{aligned}
\hat{H}_{\text{sfss}}^{\text{AIMP}} = \sum_{i=1}^{N_{\text{val}}^{\text{clus}}} &\left\{ -\frac{1}{2}\hat{\nabla}_i^2 + \sum_{\mu \in \text{clus}}^{N_{\text{nuc}}^{\text{clus}}} \left[-\frac{Z_\mu^{\text{eff}}}{r_{\mu i}} + \hat{V}_{\mu-\text{core}}^{\text{AIMP}}(i) \right. \right. \\
&\left. + \hat{h}_\mu^{\text{SO}}(i) \right] + \sum_{\xi \in \text{host}}^{N_{\text{ion}}^{\text{host}}} \hat{V}_{\xi-\text{ion}}^{\text{emb-AIMP}}(i) \Bigg\} + \sum_{i=1}^{N_{\text{val}}^{\text{clus}}} \sum_{j>i}^{N_{\text{val}}^{\text{clus}}} \frac{1}{r_{ij}} \\
&+ \sum_{\mu \in \text{clus}}^{N_{\text{nuc}}^{\text{clus}}} \sum_{\nu(>\mu) \in \text{clus}}^{N_{\text{nuc}}^{\text{clus}}} \frac{Z_\mu^{\text{eff}} Z_\nu^{\text{eff}}}{R_{\mu\nu}} + \sum_\gamma^{N_{\text{SF}}^{\mathcal{P}}} \delta_\gamma |\Phi_{\text{SF},\gamma}^{\mathcal{P}}\rangle\langle\Phi_{\text{SF},\gamma}^{\mathcal{P}}|.
\end{aligned}
\tag{1}
$$

In Eq. (1), the indices i and j refer to the $N_{\text{val}}^{\text{clus}}$ valence electrons of the cluster, μ and ν refer to the $N_{\text{nuc}}^{\text{clus}}$ nuclei (atoms) of the $(UCl_6)^{3-}$ cluster, each of them having N_μ^{core} core electrons and an effective nuclear charge $Z_\mu^{\text{eff}} = Z_\mu - N_\mu^{\text{core}}$. The ξ index refers to the $N_{\text{ion}}^{\text{host}}$ ions of the Cs_2NaYCl_6 embedding host, i.e., all the ions in the doped material except the U^{3+} impurity and its first coordination shell of six Cl^- ions.

$\hat{V}_{\mu-\text{core}}^{\text{AIMP}}(i)$ is the one-electron spin-free relativistic *ab initio* model potential,[30] which represents the effects of the core electrons of atom μ (an effective core potential) plus

the scalar Darwin and mass–velocity atomic potentials of Cowan and Griffin (which are variationally stable)[31] acting on the valence electrons. It reads

$$
\begin{aligned}
\hat{V}_{\mu-\text{core}}^{\text{AIMP}}(i) = &\frac{1}{r_{\mu i}} \sum_k C_k^\mu \exp(-\alpha_k^\mu r_{\mu i}^2) + \sum_j \sum_k |\chi_j^\mu\rangle \\
&\times A_{j,k}^\mu \langle\chi_k^\mu| + \sum_{c \in \mu-\text{core}} D_c^\mu |\phi_c^\mu\rangle\langle\phi_c^\mu|.
\end{aligned}
\tag{2}
$$

The first term in the right-hand side of Eq. (2) is the core Coulomb model potential, which is produced by least-squares fitting to the true core Coulomb potential of atom μ.[32] The second term is the core exchange, plus Darwin, plus mass–velocity model potential, which is produced by the spectral representation of the true operators in the space defined by the one-center basis set $\{|\chi_j^\mu\rangle\}$;[32] this basis set is chosen to be the set of Gaussian primitive functions used in the embedded cluster calculation that are centered on atom μ. The third term is the core shifting operator of Huzinaga and Cantu[33] that prevents the valence orbitals from collapsing onto the core orbitals.

$\hat{h}_\mu^{\text{SO}}(i)$ is the one-electron spin–orbit model potential.[23] It results from the true spin–orbit operator of Wood and Boring,[22] after using: (a) a suitable analytical representation of the radial components of the Wood–Boring spin–orbit operator, produced by least-squares fitting, and (b) an angular projection of the atomic $\hat{\ell}^\mu \hat{s}$ operator according to Pitzer and Winter.[34] It reads

$$
\begin{aligned}
\hat{h}_\mu^{\text{SO}}(i) = &\lambda_\mu \sum_{n\ell \in \mu-\text{val}} \frac{\sum_k B_k^{n\ell,\mu} \exp(-\beta_k^{n\ell,\mu} r_{\mu i}^2)}{r_{\mu i}^2} \\
&\times \hat{O}_\ell^\mu \hat{\ell}^\mu \hat{s} \hat{O}_\ell^\mu,
\end{aligned}
\tag{3}
$$

where the angular projection operator $\hat{O}_\ell^\mu$ is defined in terms of the spherical harmonics centered on μ

$$
\hat{O}_\ell^\mu = \sum_{m=-\ell}^{+\ell} |Y_{\ell m}^\mu\rangle\langle Y_{\ell m}^\mu|.
\tag{4}
$$

Since the Wood–Boring spin–orbit coupling operator leads to systematic overestimations of the atomic spin–orbit coupling constants of around 10%,[23] we use a spin–orbit atomic scaling factor λ_μ in Eq. (3). In this paper we use $\lambda_U = 0.9$, which has been found to be good for the $5f^2$ manifold of U^{4+}-doped Cs_2ZrCl_6.[20]

$\hat{V}_{\xi-\text{ion}}^{\text{emb-AIMP}}(i)$ is the contribution of the host ion ξ to the one-electron embedding model potential.[21] It reads

$$
\begin{aligned}
\hat{V}_{\xi-\text{ion}}^{\text{emb-AIMP}}(i) = &-\frac{Q_\xi}{r_{\xi i}} + \frac{1}{r_{\xi i}} \sum_k C_k^\xi \exp(-\alpha_k^\xi r_{\xi i}^2) \\
&+ \sum_j \sum_k |\chi_j^\xi\rangle A_{j,k}^\xi \langle\chi_k^\xi| \\
&+ \sum_{c \in \xi-\text{ion}} D_c^\xi |\phi_c^\xi\rangle\langle\phi_c^\xi|.
\end{aligned}
\tag{5}
$$

This single-ion embedding model potential is isomorphous with the core model potential, Eq. (2), except for the presence of the term $-Q_\xi/r_{\xi i}$, which represents the long-range Coulomb (Madelung) potential created by a point charge Q_ξ (the ionic charge.) The next two terms of this model potential are approximations, respectively, to the short-range Coulomb potential of the full ion (which is defined as the Coulomb potential of the full ion minus the long-range Coulomb potential) and to the full ion exchange operator. They are produced like the corresponding terms in Eq. (2). The last term in Eq. (5) is the full ion shifting operator, which prevents the cluster wave functions from collapsing onto this particular lattice ion.[33]

The last term in Eq. (1) is a spin-free-state-shifting operator.[24] Based on the ideas of Teichteil *et al.*,[35] it is a practical means to transfer large amounts of electron correlation effects from a sophisticated calculation with a spin-free Hamiltonian (e.g., a CI calculation within a very large $\mathcal{G}$ configuration space) to a much simpler calculation with a spin–orbit Hamiltonian (e.g., a spin–orbit CI calculation within a small $\mathcal{P}$ configuration space). In it, $|\Phi_{SF,\gamma}^{\mathcal{P}}\rangle$ is the wave function of state γ that corresponds to the small space $\mathcal{P}$ and to the spin-free Hamiltonian. The shifting coefficient δ_γ is calculated using the energies of state γ and of a reference state 0 (usually the ground state,) corresponding to the spin-free Hamiltonian, as calculated within a small configuration space $\mathcal{P}$: $E_0^{\mathcal{P}}$ and $E_\gamma^{\mathcal{P}}$, and within a large configuration space $\mathcal{G}$: $E_0^{\mathcal{G}}$ and $E_\gamma^{\mathcal{G}}$

$$\delta_\gamma = [E_\gamma^{\mathcal{G}} - E_0^{\mathcal{G}}] - [E_\gamma^{\mathcal{P}} - E_0^{\mathcal{P}}]. \qquad (6)$$

$N_{SF}^{\mathcal{P}}$ is the number of states of the spin-free Hamiltonian included in the shifting operator. Although its choice is arbitrary, the projection of the final wave functions of the spin–orbit Hamiltonian on the space spanned by the $N_{SF}^{\mathcal{P}}$ wave functions $|\Phi_{SF,\gamma}^{\mathcal{P}}\rangle$ can be used for a systematic evaluation of $N_{SF}^{\mathcal{P}}$.[36] Our choice here makes the projection of all the states of interest to be larger than 99.95%.

B. Details of the calculations

In addition to the $5f^2 6d^1$ manifold of the $(UCl_6)^{3-}$ cluster embedded in Cs$_2$NaYCl$_6$, we also calculated the parent excited states of the U^{3+} free ion, which are useful for interpretation. In both systems, the calculations were done in two steps: In a first step, in which all the relevant electron correlation effects are the main focus of attention, the spin-free Hamiltonian was used

$$\hat{H}_{\text{spin-free}}^{\text{AIMP}} = \hat{H}_{\text{sfss}}^{\text{AIMP}} - \sum_{\gamma}^{N_{SF}^{\mathcal{P}}} \delta_\gamma |\Phi_{SF,\gamma}^{\mathcal{P}}\rangle \langle \Phi_{SF,\gamma}^{\mathcal{P}}|$$
$$- \sum_{i=1}^{N_{\text{val}}^{\text{clus}}} \sum_{\mu \in \text{clus}}^{N_{\text{nuc}}^{\text{clus}}} \hat{h}_\mu^{\text{SO}}(i), \qquad (7)$$

which is formally identical to a nonrelativistic Hamiltonian; we performed this step with the MOLCAS-5 package.[37] In a second step, in which the main interest is shifted towards spin–orbit coupling effects, the spin–orbit Hamiltonian

$\hat{H}_{\text{sfss}}^{\text{AIMP}}$ [Eq. (1)] was used; we performed this step with a modified version of the COLUMBUS package.[38]

The [Xe,4f] core AIMPs of neutral actinoids were found to be appropriate for the $5f^n$ and $5f^{n-1}6d^1$ manifolds of actinide ions;[39] accordingly, we used the [Xe,4f] core AIMP [Eq. (2)] of neutral U $(5f^3 6d^1 7s^2)^5 K$.[39,40] We used a $(14s10p12d9f3g)/[6s4p5d4f2g]$ Gaussian valence basis set for U (see Sec. II C). For Cl, we used the [Ne] core AIMP[30] together with a valence basis set $(7s7p1d)$ contracted as $[3s4p1d]$, which resulted from the minimal $(7s6p)$ basis set of Ref. 30 upon split, and addition of one p diffuse function for anions[41] and one d polarization function.[42] The d polarization functions of Cl and the g polarization functions of U were formally removed in the spin–orbit calculations; note, however, that their effects on the spin–orbit states are taken into account by means of the spin-free-state-shifting operator.

We used the Cs$_2$NaYCl$_6$ AIMP embedding potential of Ref. 43, which was produced in *self-consistent embedded ions* calculations; it is made of a sum of 482 single-ion AIMPs [Eq. (5)] of the Cs$^+$, Na$^+$, Y^{3+}, and Cl$^-$ ions surrounding the cluster, plus 2696 extra point charges that allow for a correct description of the long-range Madelung potential; all of the single-ion AIMPs and point-charges are located at experimental sites [Cs$_2$NaYCl$_6(O_h^5$-$F_{m3m})$, $a = 10.7396$ Å, $x_{Cl} = 0.243\,93$.][44]

The two-step calculations on free U^{3+} ion were done as follows: We performed spin-free Hamiltonian CASSCF calculations (with an active space defined by all possible distributions of 3 electrons in 13 active atomic orbitals $5f$, $6d$, and $7s$) in the average of all doublets from 1^2H to 2^2H and all quartets from ^4K to 2^4G of the $5f^2 6d^1$ manifold, followed by MS-CASPT2 calculations in which 11 electrons were correlated (those in the active orbitals and in the $6s$ and $6p$ closed-shells). In the second step, we performed spin–orbit Hamiltonian spin-free-state-shifted MRCI(S) calculations in which only single excitations from the $5f$ and $6d$ atomic orbitals to the virtual space were allowed from the CAS multireference (the $\mathcal{P}$ space;) the atomic orbitals optimized in the SA-CASSCF calculations were used here. This kind of spin–orbit CI calculations has been found to be sufficient for a good description of spin–orbit splittings.[36] The $E_0^{\mathcal{G}}$ and $E_\gamma^{\mathcal{G}}$ energies in the shifting coefficients δ_γ [Eq. (6)] were calculated with the MS-CASPT2 results and they are shown in Table I.

In the $(UCl_6)^{3-}$ octahedral cluster embedded in Cs$_2$NaYCl$_6$, we first performed spin-free Hamiltonian state average complete active space self-consistent field calculations, SA-CASSCF,[25] with 3 electrons in 13 active molecular orbitals with main character U $5f$, $6d$, and $7s$ (a_{2u}, t_{2u}, t_{1u}, t_{2g}, e_g, and a_{1g}) which we will call SA-CASSCF [$5f,6d,7s$].[3] Four sets of molecular orbitals were produced for each nuclear configuration, each in a separated SA-CASSCF calculation: (a) MOs that minimize the average energy of all $^4A_{1g}$, $^4A_{2g}$, and ^4E_g states up to 3 $^4A_{1g}$, 5 $^4A_{2g}$, and 8 ^4E_g, all of them having a main configuration U $5f^2 6d^1$ [either $5f^2 6d(t_{2g})^1$ or $5f^2 6d(e_g)^1$,] the next state being of main character U $5f^2 7s^1$; (b) MOs that minimize the average energy of all $^4T_{1g}$ and $^4T_{2g}$ states up to 13 $^4T_{1g}$

TABLE I. Energy levels of the $5f^2 6d^1$ configuration of free U^{3+}. Results of MS-CASPT2 calculations ($6s$, $6p$, $5f$, and $6d$ electrons are correlated) with the spin-free Hamiltonian [Eq. (7)] and spin-free state shifted MRCI(S) calculations with the spin–orbit Hamiltonian [Eq. (1)] are presented. The values of the spin-free state shifting parameters δ_γ [Eq. (6)] used in the spin–orbit MRCI(S) calculation and the correspondence between free-ion and O_h cluster levels are also presented. All energies are in cm^{-1}. Note that all the states are *gerade*. Total (valence only) energies of the term ^4K and the lowest level $J = 11/2$ are $-217.397\,590$ and $-217.449\,429$ a.u., respectively.

| Term | Energy[a] | δ_γ [Eq. (6)] | Spin-free Hamiltonian [Eq. (7)] Related O_h spin-free states | | | | | | | | | |
			$^4A_{1g}$	$^4A_{2g}$	^4E_g	$^4T_{1g}$	$^4T_{2g}$	$^2A_{1g}$	$^2A_{2g}$	^2E_g	$^2T_{1g}$	$^2T_{2g}$
$1\ ^2H$	−3 340	−1 210						0	0	1	2	1
^4K	0	0	0	1	1	2	2					
$1\ ^2F$	700	−3 340						0	1	0	1	1
$1\ ^4G$	1 080	0	1	0	1	1	1					
^4I	1 100	0	1	1	1	1	2					
^2I	1 550	440						1	1	1	1	2
$1\ ^4H$	2 560	−550	0	0	1	2	1					
$1\ ^2D$	4 160	−3 750						0	0	1	0	1
^4P	4 230	−2 370	0	0	0	1	0					
^2P	4 410	−5 850						0	0	0	1	0
$2\ ^4H$	4 830	−4 100	0	0	1	2	1					
$1\ ^2G$	5 720	−4 180						1	0	1	1	1
$1\ ^4F$	5 970	−4 250	0	1	0	1	1					
$2\ ^2H$	6 340	−1 890						0	0	1	2	1
^4D	6 950	−5 030	0	0	1	0	1					
$2\ ^2F$	7 150	−4 890						0	1	0	1	1
$2\ ^2G$	7 540	−4 320						1	0	1	1	1
$2\ ^4G$	7 850	−3 650	1	0	1	1	1					
^2K	9 640	−2 050						0	1	1	2	2
$2\ ^4F$	10 490	−4 920	0	1	0	1	1					
$2\ ^2D$	10 700	−4 840						0	0	1	0	1

| Level[b] | Energy[c] | Spin–orbit Hamiltonian [Eq. (1)] Related $\bar{O}_h$ spin–orbit states | | |
		Γ_{6g}	Γ_{7g}	Γ_{8g}
$11/2\ (^4K\ 67,\ ^4I\ 25)$	0	1	1	2
$9/2\ (^4I\ 50,\ 1^2H\ 34)$	1 420	1	0	2
$5/2\ (1^4G\ 44,\ 1^2F\ 40)$	2 040	0	1	1
$7/2\ (1^4H\ 61,\ 1^2G\ 14)$	4 230	1	1	1
$9/2\ (1^2H\ 51,\ ^4I\ 31)$	5 320	1	0	2
$11/2\ (1^2H\ 49,\ ^4K\ 21)$	5 680	1	1	2
$13/2\ (^4K\ 90,\ ^2I\ 9)$	6 440	1	2	2
$1/2\ (^2P\ 55,\ ^4D\ 22)$	6 480	1	0	0
$7/2\ (2^4H\ 44,\ 1^4G\ 29)$	7 030	1	1	1
$7/2\ (2^4H\ 35,\ 1^4G\ 33)$	7 850	1	1	1
$11/2\ (^4I\ 84,\ 2^2H\ 7)$	8 000	1	1	2
$5/2\ (1^4G\ 40,\ 1^2D\ 30)$	9 380	0	1	1
$9/2\ (1^4H\ 81,\ 1^4G\ 7)$	9 570	1	0	2
$3/2\ (1^4P\ 38,\ ^2P\ 24)$	10 700	0	0	1
$9/2\ (2^4H\ 36,\ 1^4G\ 17)$	11 190	1	0	2
$5/2\ (2^4G\ 27,\ 1^4F\ 27)$	11 300	0	1	1
$3/2\ (1^4F\ 77,\ 1^2D\ 10)$	11 670	0	0	1

[a]Relative to $5f^2 6d^1 - {}^4K$, which is 30 850 cm^{-1} above the $5f^3 - {}^4I$ ground term.
[b]The values of J are indicated, together with the leading term characters, in percentage.
[c]Relative to lowest state of the $5f^2 6d^1$ configuration, $J = 11/2$ (^4K), which is 27 940 cm^{-1} above the $5f^3\ J = 9/2$ (^4I) ground state.

and 12 $^4T_{2g}$, which includes U $5f^2 6d(t_{2g})^1$ and U $5f^2 6d(e_g)^1$ states; (c) MOs that minimize the average energy of all $^2A_{1g}$, $^2A_{2g}$, and ^2E_g states up to 3 $^2A_{1g}$, 2 $^2A_{2g}$, and 5 ^2E_g (included in an energy window of around 12 000 cm^{-1}, the next state of these irreducible representations being 3000 cm^{-1} above) and (d) MOs that minimize the average energy of all $^2T_{1g}$ and $^2T_{2g}$ states up to 7 $^2T_{1g}$ and 8 $^2T_{2g}$ (included in an energy window of around 13 000 cm^{-1}, the next state of these irreducible representations being 1000 cm^{-1} above). The CAS-CI energies of all the states of the

given irreducible representations have been calculated using their corresponding MOs. All this produces structural and spectroscopic results at a CASSCF level, but it also produces the necessary ingredients for MS-CASPT2 calculations.[26–29] The MS-CASPT2 calculations performed include dynamic correlation of 11 electrons occupying the active MOs and the MOs with main character U $6s$ and U $6p$, plus 48 electrons occupying MOs with main ligand character Cl $3s$ and Cl $3p$. These calculations are labeled MS-CASPT2(Cl48,U11). All these methodological choices are justified in Sec. II C. Fi-

nally, we performed spin–orbit Hamiltonian spin-free-state-shifted MRCI(S) calculations. The CI space was defined by the CAS multireference plus all single excitations from the MOs with main character U $5f$ and U $6d$. Here, the CASSCF MOs and the shifting coefficients δ_γ corresponding to the MS-CASPT2(Cl48,U11) results were used. The spin–orbit potentials [Eq. (3)] were taken from Refs. 40 (U) and 45 (Cl).

C. Active space, basis set, and dynamic correlation

In this section, we present the results of a numerical study addressed to establish methodological conditions which are appropriate for practical studies of $5f^3$ and $5f^26d^1$ manifolds of $(UCl_6)^{3-}$, meaning that they fulfill conditions of acceptable precision at a reasonable computational cost. We consider here the active space, the basis set of U, and the dynamic correlation. We expect the conclusions of this section to be transferable to the $5f^n$ and $5f^{n-1}6d^1$ manifolds of other actinide ion halides.

SA-CASSCF calculations in Cs$_2$NaYCl$_6$: $(UCl_6)^{3-}$ with an active space resulting from distributing 3 electrons in 12 active molecular orbitals with main character U $5f$ and $6d$, SA-CASSCF $[5f,6d]^3$, lead to results of U–Cl bond distances, breathing mode frequencies, minimum-to-minimum energy differences, and vertical (Franck–Condon) energy differences, essentially coincident with those of SA-CASSCF $[5f,6d,7s]^3$ calculations. However, all the CASPT2 calculations with the SA-CASSCF $[5f,6d]^3$ reference lead to a number of intruder states that contaminate the results of several excited states. The contaminated states were different for different basis sets and for different choices of zero-order Hamiltonian, but there were always some intruder states. They were fully removed after including in the CAS space the MO with main character U $7s$, that is, by using a SA-CASSCF $[5f,6d,7s]^3$ reference. Accordingly, the results presented in this paper correspond to a $[5f,6d,7s]^3$ complete active space of $(UCl_6)^{3-}$. We expect this CAS to be also necessary for other 3+ actinide ions. We may mention that including the U $7s$ orbital in the active space was not found to be necessary for U^{4+} hexachloride,[20] where the energy difference between $6d$ and $7s$ is larger.

The $[6s5p6d4f]$ contraction of the $(14s10p12d9f)$ primitive Gaussian basis set corresponding to the [Xe,$4f$] core was recommended for molecules containing actinide elements.[39] In the case of $5f^n$ and $5f^{n-1}6d^1$ configurations of multiply ionized actinides like U^{3+}, where the $7s$ orbital is empty and $6d$ orbitals more compact than in neutral atoms are present, smaller contractions of the basis set might be useful. The results of a systematic study on the basis set contraction are shown in Table II, where the effects of additional g polarization functions are also shown (by addition of the outermost primitives to a $3g$ contracted function produced by maximum radial overlap with the $5f$ orbital of U). In the table, we present SA-CASSCF $[5f,6d,7s]^3$ calculations as well as two sets of MS-CASPT2 calculations: one which includes dynamic correlation of the 3 electrons in the active MOs plus the 36 electrons in MOs with main character Cl $3p$ (Cl36,U3), and a second one with additional dynamic correlation from the U $6s$ and $6p$, and Cl $3s$ electrons

(Cl48,U11), so that the effects of dynamic correlation can also be shown. We calculated the following states of the spin-free Hamiltonian of Cs$_2$NaYCl$_6$: $(UCl_6)^{3-}$ at $r(U–Cl) = 2.752$ Å: $5f^3 - 1\ ^4E_u(^4I)$, $5f^3 - 1\ ^4A_{2u}(^4I)$, $5f^3 - 2\ ^4A_{1u}(^4S)$, $5f^26d(t_{2g})^1 - 1\ ^4A_{2g}$, and $5f^26d(e_g)^1 - 4\ ^4A_{2g}$. With the first two, we can monitor the effects on two states related to the same atomic term, that is, the effects on the $5f$ crystal field splitting; the third one allows one to monitor the effects on a $5f\to5f$ transition connecting two states related to different atomic terms; the fourth state gives the effects on a $5f\to6d$ transition, and, finally, the fifth state allows one to know the effects on the $6d$ crystal-field splitting $(t_{2g}-e_g)$, by comparison with the fourth.

In Table II we observe very small effects of addition of one f primitive to the $[6s5p6d4f]$ set, as well as of reduction of one p and d primitives, whatever the level of calculation is. The only significant effect of the reduction of one s primitive is a small increase of almost 500 cm^{-1} in the $5f\to6d$ transitions; even though this is acceptable, we take the $[6s4p5d4f]$ set as a basis for further experimentation with g functions. These g functions are insignificant at the CASSCF level of calculation, with a maximum effect of 100 cm^{-1}. However, they become relevant for dynamic correlation: in effect, at the MS-CASPT2 (Cl36,U3) level they increase by 1500 cm^{-1} the $5f\to6d(t_{2g})$ transition and lower by approximately 1300 cm^{-1} the $6d$ crystal field splitting; at the (Cl48,U11) level these increments become 4500 and 1200 cm^{-1}, approximately. The $(14s10p12d9f3g)/[6s4p5d4f2g]$ results do not essentially change upon addition of one extra g functions; this seems to be a good choice of basis set. Finally, by comparing (Cl36,U3) and (Cl48,U11) results, its is clear that dynamic correlation from Cl $3s$ and U $6s$ and $6p$ orbitals should not be neglected for the states under study.

III. RESULTS

A. U^{3+}

The calculated levels of the $5f^26d^1$ configuration of U^{3+} are shown in Fig. 1 and Table I, where the analysis in terms of SL functions is included. Experimental data on these levels are not available in the literature to the best of our knowledge. Although the lowest term of the spin-free Hamiltonian is ^2H, which is 3340 cm^{-1} more stable than ^4K, the large spin–orbit coupling stabilizes the spin quartet states and the four lowest states show main contributions from ^4K, ^4I, $1\ ^4G$, and $1\ ^4H$. These lowest states have $J = 11/2$, $9/2$, $5/2$, and $7/2$, respectively. The next two states, with $J=9/2$ and $11/2$, show dominant spin doublet character ($1\ ^2H$) and the next one is mainly the $J=13/2$ spin–orbit component of ^4K. The first state, $J=11/2$ (^4K), is 27 940 cm^{-1} above the $5f^3$ $J=9/2$ (^4I) ground state, and the next states with dominant quartet character are separated by 1420, 620, 2190, and 2210 cm^{-1}. As we will comment below, the absorption spectrum of U^{3+}-doped Cs$_2$NaYCl$_6$ is related to these states according to our interpretation.

TABLE II. Basis set and dynamic correlation effects on selected transitions of Cs_2NaYCl_6:$(UCl_6)^{3-}$ with $r(U–Cl)=2.752$ Å. The complete active space of all calculations corresponds to the distribution of 3 electrons in the 13 MOs with main character U $5f$, $6d$, and $7s$. All energies in cm^{-1}.

Basis set contraction	$5f^3-1\,^4E_u(^4I) \rightarrow$	SA-CASSCF	MS-CASPT2 (Cl36,U3)	MS-CASPT2 (Cl48,U11)
Primitive set $(14s10p12d9f)$				
$[6s5p6d4f]$	$\rightarrow 1\,^4A_{2u}(^4I)$ [a]	-512	356	835
	$\rightarrow 2\,^4A_{1u}(^4S)$ [b]	8 686	7 877	6 754
	$\rightarrow 1\,^4A_{2g}$ [c]	12 470	9 070	11 110
	$\rightarrow 4\,^4A_{2g}$ [d]	34 850	29 400	27 730
	$1\,^4A_{2g}\rightarrow 4\,^4A_{2g}$ [e]	22 380	20 330	16 620
$[6s5p6d5f]$	$\rightarrow 1\,^4A_{2u}$	-512	360	838
	$\rightarrow 2\,^4A_{1u}$	8 684	7 872	6 746
	$\rightarrow 1\,^4A_{2g}$	12 460	9 120	11 170
	$\rightarrow 4\,^4A_{2g}$	34 860	29 430	27 770
	$1\,^4A_{2g}\rightarrow 4\,^4A_{2g}$	22 400	20 310	16 600
$[6s4p6d4f]$	$\rightarrow 1\,^4A_{2u}$	-510	312	820
	$\rightarrow 2\,^4A_{1u}$	8 697	7 982	6 885
	$\rightarrow 1\,^4A_{2g}$	12 640	9 200	11 230
	$\rightarrow 4\,^4A_{2g}$	35 040	29 570	27 910
	$1\,^4A_{2g}\rightarrow 4\,^4A_{2g}$	22 400	20 370	16 680
$[6s4p5d4f]$	$\rightarrow 1\,^4A_{2u}$	-509	315	833
	$\rightarrow 2\,^4A_{1u}$	8 717	8 012	6 962
	$\rightarrow 1\,^4A_{2g}$	12 690	9 360	11 430
	$\rightarrow 4\,^4A_{2g}$	35 100	29 790	28 280
	$1\,^4A_{2g}\rightarrow 4\,^4A_{2g}$	22 410	20 430	16 850
$[5s4p5d4f]$	$\rightarrow 1\,^4A_{2u}$	-508	297	832
	$\rightarrow 2\,^4A_{1u}$	8 734	8 035	7 010
	$\rightarrow 1\,^4A_{2g}$	13 150	9 820	11 830
	$\rightarrow 4\,^4A_{2g}$	35 600	30 320	28 750
	$1\,^4A_{2g}\rightarrow 4\,^4A_{2g}$	22 450	20 500	16 920
Primitive set $(14s10p12d9f3g)$				
$[6s4p5d4f1g]$	$\rightarrow 1\,^4A_{2u}$	-595	332	953
	$\rightarrow 2\,^4A_{1u}$	8 735	7 411	6 288
	$\rightarrow 1\,^4A_{2g}$	12 680	10 850	15 970
	$\rightarrow 4\,^4A_{2g}$	35 110	29 980	31 640
	$1\,^4A_{2g}\rightarrow 4\,^4A_{2g}$	22 430	19 130	15 670
$[6s4p5d4f2g]$	$\rightarrow 1\,^4A_{2u}$	-591	403	1 069
	$\rightarrow 2\,^4A_{1u}$	8 746	7 460	6 319
	$\rightarrow 1\,^4A_{2g}$	12 610	10 480	15 550
	$\rightarrow 4\,^4A_{2g}$	35 050	29 530	31 170
	$1\,^4A_{2g}\rightarrow 4\,^4A_{2g}$	22 440	19 050	15 620
$[6s4p5d4f3g]$	$\rightarrow 1\,^4A_{2u}$	-594	381	1 108
	$\rightarrow 2\,^4A_{1u}$	8 753	7 438	6 300
	$\rightarrow 1\,^4A_{2g}$	12 620	10 570	15 800
	$\rightarrow 4\,^4A_{2g}$	35 060	29 530	31 330
	$1\,^4A_{2g}\rightarrow 4\,^4A_{2g}$	22 440	18 960	15 530

[a] $5f\rightarrow 5f$ intraterm transition.
[b] $5f\rightarrow 5f$ interterm transition.
[c] $5f\rightarrow 6d(t_{2g})$.
[d] $5f\rightarrow 6d(e_g)$.
[e] $5f^26d(t_{2g})^1-1\,^4A_{2g}\rightarrow 5f^26d(e_g)^1-4\,^4A_{2g}$, which is a measure of the $6d$ crystal field splitting, and it is very approximately the crystal field theory parameter 10Dq.

B. Cs_2NaYCl_6 : $(UCl_6)^{3-}$

First, we show in Table III a summary of the results of the spin-free Hamiltonian calculations [Eq. (7)] on the $(UCl_6)^{3-}$ cluster embedded in Cs_2NaYCl_6. These calculations are a first and necessary step in the procedure leading to

the final results which include electron correlation and spin–orbit coupling effects, but they already provide useful structural information because it does not change with spin–orbit coupling, as we will see (Table IV).

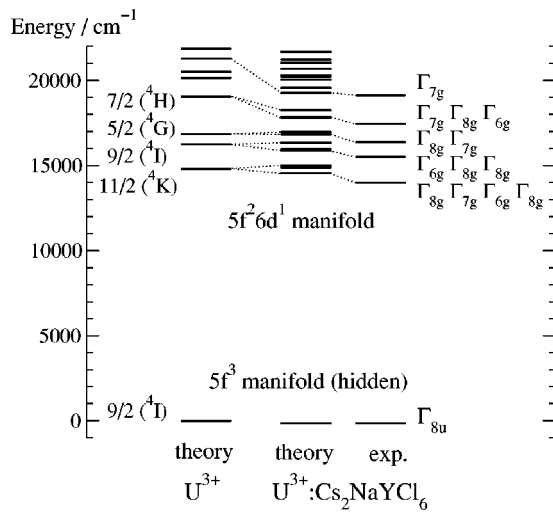At the CASSCF level (where all the embedding and

FIG. 1. Theoretical and experimental levels of the $5f^26d^1$ configuration of U^{3+}-doped Cs$_2$NaYCl$_6$. Theoretical results of free U^{3+} are also drawn, with the $5f^26d^1$ manifold shifted $-13\,115$ cm^{-1} [so that the $J=11/2$ level coincides with the center of gravity of its related (UCl$_6$)$^{3-}$ calculated levels Γ_{8g}, Γ_{7g}, Γ_{6g}, and Γ_{8g}] for the sake of clarity.

bonding interactions other than dynamic correlation and spin–orbit coupling are considered), the states can be grouped in two sets according to their bond distances: those with a dominant $5f^26d(t_{2g})^1$ configuration, with mean average 2.752 Å and standard deviation 0.002 Å, R$_e$ = (2.752 ±0.002) Å, and those with a dominant $5f^26d(e_g)^1$ configu-

ration, with R$_e$ = (2.803±0.002) Å. All the states whose only difference is the distribution of the $5f^2$ electrons have essentially the same bond distance; this is a consequence of the inner $5f$ shell being shielded from the ligands by the U $6s$ and U $6p$ shells, which makes the $5f$ crystal field splitting very small (Fig. 2). The larger bond distance of the $5f^26d(e_g)^1$ states is the consequence of the $6d$ crystal field splitting in an octahedral environment. In effect, the crystal field stabilizes the $6d(t_{2g})$ MOs of π antibonding character with respect to the $6d(e_g)$ MOs of σ antibonding character, which results in a $t_{2g} \rightarrow e_g$ energy difference (10Dq) that decreases with the metal–ligand distance (the well-known R^{-5} dependence in crystal field theory[46]); adding this to the energy versus distance curve of a $5f^26d(t_{2g})^1$ state results in a energy versus distance curve of a $5f^26d(e_g)^1$ state shifted to the right, that is, with a larger bond distance. Furthermore, the $5f^26d(t_{2g})^1$ bond distance is smaller than that of the states of the $5f^3$ configuration: R$_e$ = 2.769 Å.[47] This fact has been found in other actinide ions such as Pa^{4+}[19] and U^{4+},[20] and it seems to be mainly due to the ligand $\rightarrow f$ charge transfer, which is larger in the $5f^{n-1}6d^1$ configuration than in the $5f^n$ configuration and tends to shorten the impurity–ligand distance.[47]

The dynamic correlation effects included in the MS-CASPT2(Cl48,U11) have a significant impact on the bond distances, which are shortened by 0.07–0.08 Å (Table III) (the states of the $5f^3$ configuration have R$_e$ = 2.697 Å at this level of calculation[47]). However, even though all the dis-

TABLE III. Spectroscopic constants of the $5f^26d^1$ $2S+1=4$ and $2S+1=2$ manifolds of Cs$_2$NaYCl$_6$: (UCl$_6$)$^{3-}$ [U–Cl bond distance R$_e$(Å), breathing mode vibrational frequency $\omega_{a_{1g}}$(cm^{-1}), and minimum-to-minimum energy T$_e$(cm^{-1})] as calculated with the spin-free Hamiltonian [Eq. (7)]. Mean averages and standard deviations are shown for R$_e$ and $\omega_{a_{1g}}$, and energy ranges for T$_e$.

States	SA-CASSCF $[5f,6d,7s]^3$			MS-CASPT2(Cl48,U11)		
	R$_e$	$\omega_{a_{1g}}$	T$_e$ [a]	R$_e$	$\omega_{a_{1g}}$	T$_e$ [a]
$5f^26d^1$ $2S+1=4$ manifold						
$5f^26d(t_{2g})^1$ configuration						
$1-2\ ^4A_{1g}$, $1-4\ ^4A_{2g}$,	2.752±0.002	322±1 [b]	13 150–	2.674±0.003	317±2	14 400–
$1-6\ ^4E_g$,			39 160			33 520
$1-8\ ^4T_{1g}$, $1-7\ ^4T_{2g}$						
$5f^26d(e_g)^1$ configuration						
$3\ ^4A_{1g}$, $5\ ^4A_{2g}$,	2.803±0.002	328±3 [c]	40 300–	2.735±0.002	310±3	42 580–
$7-8\ ^4E_g$,			48 530			48 590
$9-13\ ^4T_{1g}$, $8-12\ ^4T_{2g}$						
$5f^26d^1$ $2S+1=2$ manifold						
$5f^26d(t_{2g})^1$ configuration						
$1-5\ ^2A_{1g}$, $1-4\ ^2A_{2g}$,	2.752±0.002	321±2	13 590–	2.674±0.003	318±2	15 050–
$1-8\ ^2E_g$,			36 500			32 220
$1-13\ ^2T_{1g}$, $1-12\ ^2T_{2g}$						

[a]From the equilibrium nuclear configuration of $5f^3$ $1\ ^4T_{2u}(^4I)$ calculated at the same level of theory (Ref. 47). $5f^3$ $1\ ^4T_{2u}(^4I)$ is the ground state at the MS-CASPT2 level, but it is 130 cm^{-1} above $5f^3$ $1\ ^4A_{2u}(^4I)$ at the CASSCF level.
[b]Excluding $8\ ^4T_{1g}$, $7\ ^4T_{2g}$, and $6\ ^4E_g$. $8\ ^4T_{1g}$ and $7\ ^4T_{2g}$ show a low value of $\omega_{a_{1g}}$(312 cm^{-1}) which results from the interaction with upper states of the same symmetry with dominant character $5f^26d(e_g)^1$. See table note c for comments on $6\ ^4E_g$.
[c]Excluding $7\ ^4E_g$, which shows a large value of $\omega_{a_{1g}}$(350 cm^{-1}) resulting from a very strong interaction with $6\ ^4E_g$. There is an avoided crossing between these two states, whose main configuration character switches with the U–Cl distance [$6\ ^4E_g$ is $5f^26d(e_g)^1$ at large U–Cl distances].

TABLE IV. Theoretical spectroscopic constants of the $5f^26d^1$ manifold of Cs_2NaYCl_6:$(UCl_6)^{3-}$ [U–Cl bond distance R_e(Å), breathing mode vibrational frequency $\omega_{a_{1g}}$(cm^{-1}), and minimum-to-minimum energy T_e (cm^{-1})] and experimental lines of the absorption spectrum that have been identified as zero-phonon lines of $5f \rightarrow 6d$ transitions, ΔE_{0-0} (Ref. 10). Mean averages and standard deviations are shown in parentheses.

State	R_e	$\omega_{a_{1g}}$	T_e^a	ΔE_{0-0} (expt.)	$T_e'^b$	$\Delta E'_{0-0}$ (expt.)^b
		(2.676 ± 0.001)	(317 ± 1)			
Main character $5f^2(^3H_4)\times 6d(t_{2g})^1(\Gamma_{8g})$						
From $^4K_{11/2}$						
1 Γ_{8g}	2.676	318	14 700	14 157	0	0
1 Γ_{7g}	2.676	318	15 040		340	
1 Γ_{6g}	2.677	318	15 160		460	
2 Γ_{8g}	2.677	317	15 170		470	
From $^4I_{9/2}$						
2 Γ_{6g}	2.677	316	16 040	15 682	1 340	1 525
3 Γ_{8g}	2.677	317	16 120		1 420	
4 Γ_{8g}	2.679	317	16 500		1 800	
From $^4G_{5/2}$						
5 Γ_{8g}	2.677	319	16 990	16 528	2 290	2 371
2 Γ_{7g}	2.674	318	17 130		2 430	
From $^4H_{7/2}$						
3 Γ_{7g}	2.678	318	17 980	17 600 ^{c}	3 280	3 440
6 Γ_{8g}	2.676	318	18 010		3 310	
3 Γ_{6g}	2.675	317	18 420		3 720	
Main character $5f^2(^3H_4)\times 6d(t_{2g})^1(\Gamma_{7g})$						
4 Γ_{7g}	2.675	318	19 440	19 200 ^{c}	4 740	5 040
7 Γ_{8g}	2.675	317	19 720		5 020	
4 Γ_{6g}	2.674	318	19 720		5 020	
5 Γ_{7g}	2.674	317	20 210		5 510	
8 Γ_{8g}	2.676	316	20 390		5 690	
9 Γ_{8g}	2.675	319	20 420		5 720	
Main character $5f^2$(other than $^3H_4$)$\times 6d(t_{2g})^1$						
5 Γ_{6g}	2.675	316	20 480			
10 Γ_{8g}	2.675	317	20 850			
6 Γ_{6g}	2.677	317	21 180			
6 Γ_{7g}	2.678	316	21 190			
11 Γ_{8g}	2.676	318	21 190			
7 Γ_{7g}	2.676	319	21 230			
12 Γ_{8g}	2.676	316	21 380			
13 Γ_{8g}	2.676	319	21 820			
7 Γ_{6g}	2.680	317	21 870			
8 Γ_{7g}	2.676	317	22 250			
14 Γ_{8g}	2.676	318	22 570			
15 Γ_{8g}	2.678	314	22 860			
16 Γ_{8g}	2.675	319	22 970			

^{a}From the equilibrium nuclear configuration of the ground state, as calculated in Ref. 47 at the same level of theory: $5f^3$ 1 $\Gamma_{8u}(^4I_{9/2})$, with $R_e=2.698$ Å and $\omega_{a_{1g}}=318$ cm^{-1}.
^{b}Referred to $1\Gamma_{8g}$.
^{c}Approximate data extracted from prominent peaks in Fig. 1 of Ref. 10; note that the real zero-phonon line could well correspond to weaker features peaking at 100–200 cm^{-1} lower energy.

tances and distance offsets are changed with dynamic correlation, the general picture of the CASSCF results stands: R_e $[5f^26d(t_{2g})^1] < R_e$ $[5f^3] < R_e$ $[5f^26d(e_g)^1]$. Breathing mode vibrational frequencies are only slightly lowered by dynamic correlation, which affects a bit more the $5f^26d(e_g)^1$ than the $5f^26d(t_{2g})^1$ states, the final result being a slightly larger frequency for the states of the latter configuration.

Regarding the energies of the states, we can mention two main effects of dynamic correlation in Cs_2NaYCl_6: $(UCl_6)^{3-}$: It changes the relative order of the states within each manifold (not shown in Table III,) which has an impor-

tant indirect effect on the spin–orbit results, and it slightly increases the $5f \rightarrow 6d$ transitions. Whereas the first effect is common to all the actinide impurities we have studied so far, the second one is more specific and deserves some attention. So, dynamic correlation effects on the $5f \rightarrow 6d$ transitions are: a large reduction (approx. 6500 cm^{-1}) in Pa^{4+}-doped Cs_2ZrCl_6 $(5f^1 \rightarrow 6d^1)$,[19] a much smaller reduction (approx. 4100 cm^{-1}) in U^{4+}-doped Cs_2ZrCl_6 $(5f^2 \rightarrow 5f^16d^1)$,[20] and a small increase (approx. 1200 cm^{-1}) in U^{3+}-doped Cs_2NaYCl_6 $(5f^3 \rightarrow 5f^26d^1)$. In Pa^{4+}, the reduction is interpreted as due to a larger stabilization of the $6d$–ligand electron pairs versus the $5f$–ligand pairs, caused by the fact that
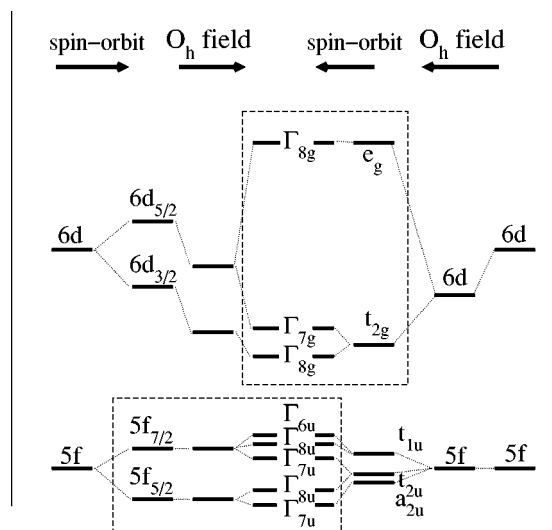
FIG. 2. Correlation diagram of the $5f$ and $6d$ one-electron levels in an octahedral field (see Ref. 19.) Boxes are used to stress the fact that the five $5f$ one-electron levels (one Γ_{6u}, two Γ_{7u}, and two Γ_{8u}) are better related to the $5f_{5/2}$ and $5f_{7/2}$ free-ion levels, whereas the three $6d$ one-electron levels (one Γ_{7g} and two Γ_{8g}) are better related to the t_{2g} and e_g crystal field split levels, because spin–orbit coupling is more important than crystal field splitting in the $5f$ shell and the opposite is true in the $6d$ shell. Note that Bethe notation is used for the Kramer's doublets of a spin–orbit O_h Hamiltonian, whereas Mulliken notation is used for the levels of the spin-free Hamiltonian, as usual.

the MOs with main character $6d$ are more extended and covalent than those with main character $5f$.[19,48,49] This effect is also present in the other ions. In U^{4+}, the $5f \rightarrow 6d$ transition means, in addition, the breaking of one $5f-5f$ pair and formation of one $5f-6d$ pair; since the electrons of the $5f-5f$ pair occupy the same region of space and those of the $5f-6d$ pair are well apart, dynamic correlation stabilizes more the $5f-5f$ pairs than the $5f-6d$ pairs and, in consequence, adds a positive contribution to a $5f \rightarrow 6d$ transition that compensates in part the stabilization commented above, the net effect of dynamic correlation being a moderate reduction of the $5f \rightarrow 6d$ transitions.[20] Here, in U^{3+}, the $5f \rightarrow 6d$ promotion means the breaking of one additional $5f-5f$ pair and formation of one $5f-6d$ pair with respect to U^{4+}, so that dynamic correlation adds a new positive contribution, the net result from the whole calculation being a small increase of the $5f \rightarrow 6d$ transitions due to dynamic correlation.

Let us now comment on the results of the spin–orbit Hamiltonian calculations [Eq. (1)] of the $5f^26d^1$ manifold of Cs_2NaYCl_6: $(UCl_6)^{3-}$, which include all the relevant interactions and are the most accurate calculations in this work. They are presented in Table IV, which shows the main features of the a_{1g} energy surfaces of the $(UCl_6)^{3-}$ cluster embedded in Cs_2NaYCl_6 of all the $5f^26d^1$ states below 23 000 cm^{-1} (U–Cl bond distance, breathing mode vibrational frequency, and minimum-to-minimum transition energies.) Table IV also shows the experimental zero-phonon lines of the 4.2 K absorption spectrum of U^{3+}-doped Cs_2NaYCl_6 taken by Karbowiak et al.,[10] which can be directly compared with the theoretical T_e values because the vibrational frequencies in the $5f^3$ and the $5f^26d^1$ states are very similar.[47]

As can be seen in Table IV, all the states in the energy region shown (14 000–23 000 cm^{-1}) have almost the same bond distance and vibrational frequency, which coincide with those of the spin-free Hamiltonian states of the $5f^26d(t_{2g})^1$ configuration. This is a consequence of the very dominant character of the $5f^26d(t_{2g})^1$ configuration in all these states, which results from the fact that the spin–orbit interactions between spin-free states of $5f^26d(t_{2g})^1$ and $5f^26d(e_g)^1$ configurations are negligible in this energy region (see Tables V and III). Since all the spin-free states of the $5f^26d(t_{2g})^1$ configuration have very similar bond distance and vibrational frequency, the spin–orbit states resulting from their mixture also have the same structural data. This means that, although demanding spin–orbit Hamiltonian calculations are compulsory in ab initio theoretical studies on the spectroscopy of these materials, simpler spin-free Hamiltonian calculations are sufficient for structural studies.

We may now compare the theoretical results with the experiments. The 4.2 K experimental absorption spectrum of Karbowiak et al.[10] in the region 14 000–23 000 cm^{-1} (Figs. 1 and 8 in Ref. 10; see also Figs. 1 and 3 in this paper) consists of several very intense and broad bands attributed to the parity-allowed $5f^3 \rightarrow 5f^26d^1$ transitions. According to the analysis of these authors, the band features are a unique example of vibronic transitions associated with this particular kind of electronic transition, and they are dominated by electric dipole vibronic satellites built on the envelope of a breathing or totally symmetric mode a_{1g}; up to the fourth member of the a_{1g} progression has been observed in the lowest electronic transitions. Three electronic origins have been detected at 14 157, 15 682, and 16 528 cm^{-1}, but the
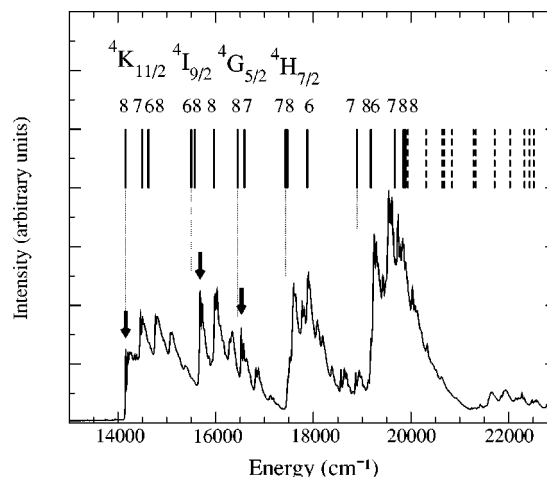

FIG. 3. Calculated energies of the lowest $5f^3$ 1 Γ_{8u} ($^4I_{9/2}$)$\rightarrow 5f^26d(t_{2g})^1$ absorption transitions. The experimental absorption spectrum at 4.2 K of Karbowiak et al. (Ref. 10) is shown, with arrows indicating three electronic origins. The theoretical levels have been shifted −540 cm^{-1} for a better display of level spacings. The numbers 6, 7, and 8 are used to label Γ_{6g}, Γ_{7g}, and Γ_{8g} levels respectively. The main free-ion character of the lowest levels is indicated; a single main character is not clear for the rest. Full lines are used for the $5f^26d(t_{2g})^1$ levels that correspond to a single electron excitation from $5f^3$ Γ_{8u} ($^4I_{9/2}$) in a simplified monoconfigurational description. The first three Γ_{6g}, three Γ_{7g}, and six Γ_{8g} levels are well described as $5f^2(^3H_4) \times 6d(t_{2g})^1(\Gamma_{8g})$ levels. The next Γ_{6g}, two Γ_{7g}, and three Γ_{8g} levels are $5f^2(^3H_4) \times 6d(t_{2g})^1(\Gamma_{7g})$ levels. The upper levels correspond to a $5f^2$ substate higher than $^3H_4$.

TABLE V. Analysis of selected spin–orbit wave functions of the $5f^2 6d(t_{2g})^1$ manifold of Cs_2NaYCl_6: $(UCl_6)^{3-}$ at R(U–Cl) = 2.70 Å, in terms of the wave functions of the spin-free Hamiltonian. Only contributions larger than 5% are shown.

State	Percentage contributions									
1 Γ_{8g}	28.82	1 $^4T_{2g}$	17.38	1 $^4A_{2g}$	16.20	1 ^4E_g	7.79	1 $^2T_{2g}$	6.03	2 $^4T_{1g}$
1 Γ_{7g}	37.96	2 $^4T_{2g}$	19.20	1 ^4E_g	10.43	2 $^2T_{2g}$	9.72	1 $^2A_{2g}$	8.00	1 $^4T_{1g}$
1 Γ_{6g}	19.79	1 $^4T_{1g}$	19.07	1 ^4E_g	16.41	2 $^4T_{1g}$	7.26	2 ^4E_g		
2 Γ_{8g}	15.16	1 $^4T_{1g}$	11.46	2 $^4T_{2g}$	9.98	2 $^4T_{1g}$	8.57	2 $^2T_{2g}$	8.39	1 ^4E_g
	6.88	1 $^4T_{2g}$	6.88	2 ^2E_g	6.50	3 $^4T_{1g}$				
2 Γ_{6g}	28.15	2 ^4E_g	21.06	3 $^4T_{2g}$	12.00	1 $^4T_{2g}$	9.52	1 $^4T_{1g}$	7.28	2 $^4T_{1g}$
	6.34	3 $^2T_{1g}$								
3 Γ_{8g}	18.17	2 ^4E_g	11.19	1 $^4T_{2g}$	9.14	1 ^2E_g	7.19	3 $^4T_{2g}$	6.26	3 $^2T_{1g}$
	6.15	1 $^2T_{2g}$	5.48	1 $^4A_{2g}$	5.16	1 $^4T_{1g}$				
4 Γ_{8g}	26.82	1 $^2T_{1g}$	11.50	1 ^2E_g	8.54	3 $^4T_{2g}$	7.89	2 $^4T_{1g}$	5.16	4 $^4T_{2g}$
5 Γ_{8g}	15.85	1 $^2T_{1g}$	11.89	1 $^4A_{1g}$	8.85	4 $^2T_{1g}$	8.82	1 $^4T_{1g}$	8.07	1 $^2T_{2g}$
	7.80	2 $^4T_{1g}$	6.52	3 $^4T_{1g}$	5.08	3 $^4T_{2g}$				
2 Γ_{7g}	15.38	1 $^4T_{1g}$	13.79	3 ^4E_g	12.02	3 $^4T_{1g}$	11.72	1 ^4E_g	11.06	4 $^4T_{1g}$
	9.31	2 $^4T_{2g}$								
3 Γ_{7g}	24.11	3 $^2T_{2g}$	21.30	3 $^4T_{1g}$	8.08	2 ^4E_g	7.72	3 ^4E_g	6.20	4 $^4T_{2g}$
	5.56	1 $^4T_{1g}$	5.14	2 $^2A_{2g}$						
6 Γ_{8g}	17.36	3 $^4T_{2g}$	12.29	4 $^4T_{1g}$	10.37	3 ^4E_g	7.72	3 $^4T_{1g}$		
3 Γ_{6g}	18.72	3 ^4E_g	16.73	2 $^4T_{1g}$	10.13	3 $^4T_{1g}$	9.35	2 $^2T_{1g}$	7.71	7 $^2T_{1g}$
	5.93	3 $^4T_{2g}$								
4 Γ_{7g}	21.05	2 $^4T_{2g}$	20.01	1 $^4T_{2g}$	17.19	1 ^4E_g	12.27	2 $^4T_{1g}$	9.75	1 $^2T_{2g}$
7 Γ_{8g}	21.76	1 $^4T_{1g}$	18.13	2 $^4T_{2g}$	10.59	1 $^4A_{2g}$	9.23	1 $^4T_{2g}$	7.87	2 $^4T_{1g}$
	7.78	2 ^4E_g	6.02	2 $^2T_{1g}$						
4 Γ_{6g}	36.99	1 ^4E_g	12.78	3 $^4T_{2g}$	8.98	2 $^4T_{1g}$	7.29	1 $^4T_{1g}$	6.03	2 $^4T_{2g}$
5 Γ_{7g}	27.42	4 $^4T_{1g}$	17.65	3 ^4E_g	9.75	1 $^4T_{1g}$	6.56	2 $^4T_{2g}$	5.80	2 $^4T_{1g}$
8 Γ_{8g}	15.58	4 $^4T_{2g}$	13.40	1 $^2T_{2g}$	8.14	6 $^4T_{1g}$	7.01	3 $^4T_{1g}$	6.94	1 ^2E_g
	6.87	3 ^2E_g	6.38	4 $^4T_{1g}$						
9 Γ_{8g}	14.84	3 $^4T_{1g}$	7.65	1 ^4E_g	7.52	4 $^4T_{1g}$	7.27	3 ^4E_g	6.79	4 $^4T_{2g}$
	6.71	1 $^4A_{1g}$	6.37	3 $^4T_{2g}$	5.60	2 $^4T_{2g}$	5.54	1 $^4A_{2g}$		

fine structure of these bands is very complex and more detailed analyses were not possible. In particular, the three mentioned origins have not been assigned and other electronic origins have not been identified. In Table IV and Fig. 1 we can see all the predicted electronic origins in the energy region experimentally studied. They are represented by vertical lines in Fig. 3. They are grouped in several sets, each of them spanning a small energy region. The first four groups correspond very well with the (small) crystal field splitting of the lowest four free ion levels of the $5f^2 6d^1$ configuration, J=11/2, J=9/2, J=5/2, and J=7/2, with main spinor configuration character $(5f_{5/2})^2(6d_{3/2})^1$ and main term character ^4K, ^4I, 1^4G, and 1^4H, respectively; after them, a very dense group of states starts that is associated with the next free ion levels, which are very close in energy (Fig. 1.) The agreement of the energies of the first electronic state of each group J=11/2, J=9/2, and J=5/2 with the three electronic origins identified experimentally is excellent (with positive deviations smaller than 550 cm^{-1}), as it is the agreement of the theoretical and the experimental spacings between these levels. Furthermore, the agreement of the energy (and the spacings) of the first state of the fourth group, J=7/2, and the first state of the fifth group with the prominent peaks at approximately 17 600 and 19 200 cm^{-1}, respectively, in Fig. 1 of Ref. 10, is also excellent. These successful comparisons support the mentioned assignments, which are detailed in Table IV.

The present theoretical results suggest that the observed absorption bands are due to vibrational structure built on multiple electronic origins rather than on single origins. This is in agreement with the fact that the fine structures of the bands are very complex and, in consequence, the detailed vibrational structure hard to extract.[10] We will try to further support this conclusion by illustrating the effect of the presence of multiple electronic origins on the band shape. In order to do so, we first calculate the a_{1g} vibrational envelope of the first absorption band assuming one single electronic origin, $5f^3 1\Gamma_{8u} (^4I_{9/2}) \rightarrow 5f^2 6d(t_{2g})^1 1\Gamma_{8g} (^4K_{11/2})$. [We use the semiclassical time-dependent approach of Heller,[50,51] with bond distances and a_{1g} vibrational frequencies taken from Table IV. Detailed formulas can be found in Refs. 19 and 52.] The result is shown in Fig. 4(a), where it is compared with the experimental absorption band profile after arbitrarily adjusting the height of the calculated zero-phonon line (ZPL) to the experiment. The disagreement is quite clear. But if we consider, first, that the (reasonable) difference between the theoretical value of $\omega_{a_{1g}}$ (318 cm^{-1}) and the experimental (approximately 300 cm^{-1}) cannot be responsible because $\omega_{a_{1g}}$ affects the bandwidth but it does not affect the relative peak heights, and secondly, that the bond distance offset between states is a property that the present method consistently calculates with quite considerable precision in transition metal impurities[18,43] and in actinide impurities such as Pa^{4+},[19] the only suspicious source for such a large mismatch between calculated and experimental band shapes is the presence of more electronic origins. So, in a second calculation we added with equal weights the previous
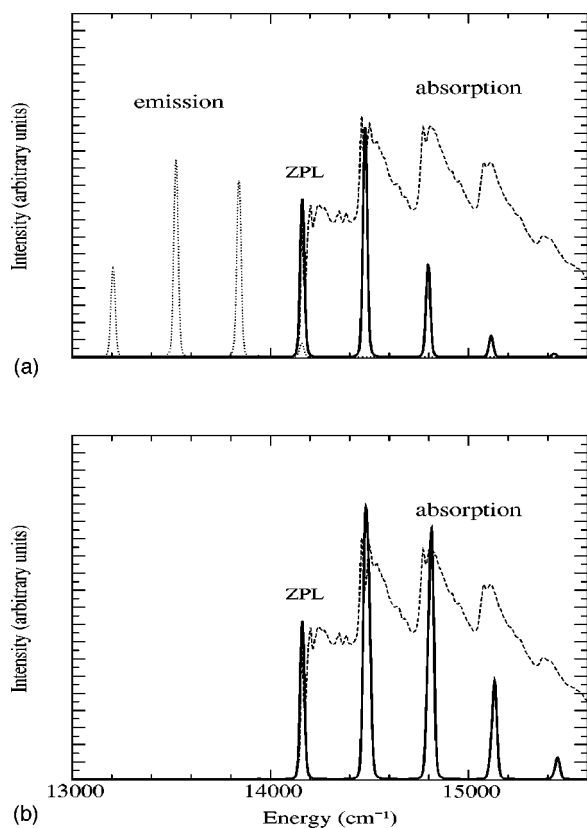
FIG. 4. Shape of the lowest observed $5f^3 \, 1\Gamma_{8u} \, (^4I_{9/2}) \rightarrow 5f^26d(t_{2g})^1$ absorption band. The experimental data at 4.2 K of Karbowiak *et al.* (Ref. 10) are shown as dashed lines. (a) Calculated a_{1g} progression built on the first $1\Gamma_{8g}$ electronic origin (full line); the corresponding $5f^26d(t_{2g})^1 \, 1\Gamma_{8g} \rightarrow 5f^3 \, 1\Gamma_{8u} \, (^4I_{9/2})$ emission is also shown (dotted line). (b) Calculated a_{1g} progressions built on the $1\Gamma_{8g}$ and $1\Gamma_{7g}$ electronic origins.

profile and the one built on the second electronic origin, $5f^3 \, 1\Gamma_{8u} \, (^4I_{9/2}) \rightarrow 5f^26d(t_{2g})^1 \, 1\Gamma_{7g} \, (^4K_{11/2})$, which is 340 cm^{-1} above the first one; the result is shown in Fig. 4(b). It is clear that the agreement has significantly improved. The large similarity between the a_{1g} vibrational frequency and the energy difference between the two electronic origins makes the resulting envelope look like a wider band built on a single origin; in particular, according to this interpretation, the fifth peak of this band is the $v=3$ a_{1g} phonon of the second electronic origin, $1\Gamma_{7g}$, rather than the $v=4$ a_{1g} phonon of the first electronic origin, $1\Gamma_{8g}$. The presence of two more (quasidegenerate) electronic origins, $1\Gamma_{6g}$ and $2\Gamma_{8g}$ could explain the remaining differences. In Fig. 4(a) we also show the calculated $5f^26d(t_{2g})^1 \, 1\Gamma_{8g} \rightarrow 5f^3 \, 1\Gamma_{8u} \, (^4I_{9/2})$ emission profile, which shows a zero-phonon line with very low intensity. No experimental $6d \rightarrow 5f$ emission spectra of U^{3+}-doped Cs₂NaYCl₆ have been published, to the best of our knowledge.

Let us now comment on the fact that no new intense bands are observed after the absorption band starting at 19 200 cm^{-1} and ending in 21 000 cm^{-1}, in spite of the fact that many $5f^26d^1$ states exist in that energy region. The ground state of the U^{3+} impurity defect in Cs₂NaYCl₆ results from the crystal field splitting of the free U^{3+} state $5f^3 \, ^4I_{9/2}$, which is the most stable state resulting from $5f^2(^3H_4) \times 5f^1$ coupling. Then, the lowest $5f \rightarrow 6d$ single-

electron excitation leads to a manifold of states that can be described in a simplified manner as $5f^2(^3H_4) \times 6d^1$. All other excitations formally described as $5f \rightarrow 6d$ and leading to manifolds such as $5f^2(^3F_2) \times 6d^1$, $5f^2(^3H_5) \times 6d^1, \ldots$, (where the two $5f$ electrons are in an excited distribution) are, rather, two-electron excitations $5f \rightarrow 6d$ and $5f \rightarrow 5f$. In consequence, the electric dipole moments should only have second-order contributions because the electric dipole operator is a one-electron operator, and their intensity should be much smaller. According to this, a first set of intense absorptions to the states of the $5f^2(^3H_4) \times 6d(t_{2g})^1(\Gamma_{8g})$ configuration should be observed; they result from the direct product of the O_h irreducible representations corresponding to $J=4$ and Γ_{8g}: $(A_{1g}+E_g+T_{1g}+T_{2g}) \times \Gamma_{8g} = 3\,\Gamma_{6g}+3\,\Gamma_{7g}+6\,\Gamma_{8g}$. These irreducible representations are found in the first four groups in Table IV, which correspond to the bands between 14 000 and 18 500 cm^{-1} in Fig. 3. Then, a second set of intense absorptions to the states of the $5f^2(^3H_4) \times 6d(t_{2g})^1(\Gamma_{7g})$ configuration should also be observed: $(A_{1g}+E_g+T_{1g}+T_{2g}) \times \Gamma_{7g} = 1\,\Gamma_{6g}+2\,\Gamma_{7g}+3\,\Gamma_{8g}$. These irreducible representations are found in the fifth group in Table IV, which corresponds to the band between 19 000 and 21 000 cm^{-1} in Fig. 3. No more intense bands should be observable in this energy region because other states of the $5f^26d(t_{2g})^1$ configuration correspond, at least, to double electron excitations. They are represented with dashed lines in Fig. 3. The next intense bands should belong to the $5f^26d(e_g)^1$ configuration (3 Γ_{6g}, 3 Γ_{7g}, and 6 Γ_{8g} origins) and they are predicted to be above 42 000 cm^{-1} if spin–orbit coupling stabilizes in similar amounts the lowest states of the $5f^3$ and $5f^26d(e_g)^1$ configurations.

IV. CONCLUSIONS

We have performed wave function based *ab initio* calculations of the large $5f^26d^1$ manifold of free U^{3+} ion and of the $(UCl_6)^{3-}$ embedded cluster, using the CASSCF, MS-CASPT2, and CI methods and a reliable representation of the Cs₂NaYCl₆ elpasolite host, with the attention focused on the structure of the U^{3+} impurity defect in those excited states and on the related spectroscopy. All the relevant effects in these materials/properties have been included: scalar and spin–orbit coupling relativistic effects, bonding interactions within the $(UCl_6)^{3-}$ cluster including nondynamic and dynamic correlation, and classical and quantum host embedding effects.

A Gaussian valence basis set for uranium of size $[6s4p5d4f2g]$, to be used together with an effective [Xe-$4f$] core potential (AIMP), meets reasonable requirements of precision and economy for this demanding manifold. An orbital active space which includes the MOs with dominant character uranium $5f$, $6d$, and $7s$ is necessary for precision and for avoiding intruder states in CASPT2 calculations. Dynamic correlation from Cl $3s$ and $3p$, and from U $6s$, $6p$, $5f$, $6d$, and $7s$ is important for a high precision of the $5f \rightarrow 6d$ transition energies.

The states of the $5f^26d^1$ manifold of Cs₂NaYCl₆: $(UCl_6)^{3-}$ are grouped in two sets according to their bond distance, which is basically independent of the spin–orbit coupling: those of the $5f^26d(t_{2g})^1$ configuration (R_e= 2.674

Å) and those of the $5f^2 6d(e_g)^1$ configuration ($R_e = 2.735$ Å), which are, respectively, shorter and larger than the bond distance in the $5f^3$ configuration ($R_e = 2.697$ Å).

The interpretation of Karbowiak *et al.*[10] of the bands of the 4.2 K absorption spectrum of U^{3+}-doped Cs_2NaYCl_6 in the energy region 14 000–21 000 cm^{-1} as due to $5f \rightarrow 6d$ transitions in U^{3+} is definitely supported by the spectroscopic calculations performed in this paper: The absolute values of the calculated transition energies and of the energy separation between the transitions show an excellent agreement with the experiments. Besides, the three unidentified electronic origins that have been detected are now assigned, and the three corresponding absorption bands are interpreted as due to the superposition of the vibronic structures built on multiple electronic origins. An interpretation is also provided for the two additional absorption bands with electronic origins observed at approximately 17 600 and 19 200 cm^{-1}, as well as for the fact that no other intense absorption bands are observed above them (and below 45 000 cm^{-1}).[10]

As a more general conclusion, we can say that this and other recent papers reporting the results of theoretical studies on actinide ion impurities doping ionic hosts show that wave function-based *ab initio* methods are capable of providing useful structural and spectroscopic information for these materials. The information complements that produced in experimental studies and gives insight to the complexity of the large manifolds of $5f^{n-1} 6d^1$ excited states, which are characteristic of these materials and are involved in physical processes of practical and basic interest.

ACKNOWLEDGMENTS

[1] H. M. Crosswhite, H. Crosswhite, W. T. Carnall, and A. P. Paszek, J. Chem. Phys. **72**, 5103 (1980).

[2] M. Karbowiak, J. Drozdzynski, K. M. Murdoch, N. M. Edelstein, and S. Hubert, J. Chem. Phys. **106**, 3067 (1997).

[3] J. Ehrlich, P. F. Moulton, and R. M. Osgood, Jr., Opt. Lett. **4**, 117 (1979).

[4] M. Nikl, Phys. Status Solidi A **178**, 595 (2000).

[5] V. N. Makhov, N. M. Khaidukov, N. Y. Kirikova, M. Kirm, J. C. Krupa, T. V. Ouvarova, and G. Zimmerer, J. Lumin. **87**, 1005 (2000).

[6] I. Sokólska and S. Kück, Chem. Phys. **270**, 355 (2001).

[7] P. A. Tanner, C. S. K. Mak, and M. D. Faucher, Chem. Phys. Lett. **343**, 309 (2001).

[8] M. Laroche, M. Bettinelli, S. Girard, and R. Moncorgé, Chem. Phys. Lett. **311**, 167 (1999).

[9] P. J. Deren, W. Strek, E. Zych, and J. Drozdzynski, Chem. Phys. Lett. **332**, 308 (2000).

[10] M. Karbowiak, J. Drozdzynski, S. Hubert, E. Simoni, and W. Strek, J. Chem. Phys. **108**, 10181 (1998).

[11] D. Piehler, W. K. Kot, and N. Edelstein, J. Chem. Phys. **94**, 942 (1991).

[12] N. Edelstein, W. K. Kot, and J. C. Krupa, J. Chem. Phys. **96**, 1 (1992).

[13] K. M. Murdoch, R. Cavellec, E. Simoni, M. Karbowiak, S. Hubert, M. Illemassene, and N. M. Edelstein, J. Chem. Phys. **108**, 6353 (1998).

[14] S. Matsika and R. M. Pitzer, J. Phys. Chem. A **104**, 4064 (2000).

[15] S. Matsika, R. M. Pitzer, and D. T. Reed, J. Phys. Chem. A **104**, 11983 (2000).

[16] S. Matsika and R. M. Pitzer, J. Phys. Chem. A **105**, 637 (2001).

[17] S. Matsika, Z. Shang, S. R. Brozell, J.-P. Blaudeau, Q. Wang, and R. M. Pitzer, J. Phys. Chem. A **105**, 3825 (2001).

[18] L. Seijo and Z. Barandiarán, in *Computational Chemistry: Reviews of Current Trends*, edited by J. Leszczynski (World Scientific, Singapore, 1999), Vol. 4, p. 55.

[19] L. Seijo and Z. Barandiarán, J. Chem. Phys. **115**, 5554 (2001).

[20] Z. Barandiarán and L. Seijo, J. Chem. Phys. (to be published).

[21] Z. Barandiarán and L. Seijo, J. Chem. Phys. **89**, 5739 (1988).

[22] J. H. Wood and A. M. Boring, Phys. Rev. B **18**, 2701 (1978).

[23] L. Seijo, J. Chem. Phys. **102**, 8078 (1995).

[24] R. Llusar, M. Casarrubios, Z. Barandiarán, and L. Seijo, J. Chem. Phys. **105**, 5321 (1996).

[25] B. O. Roos, P. R. Taylor, and P. E. M. Siegbahn, Chem. Phys. **48**, 157 (1980); P. E. M. Siegbahn, A. Heiberg, J. Almlöf, and B. O. Roos, J. Chem. Phys. **74**, 2384 (1981); P. Siegbahn, A. Heiberg, B. Roos, and B. Levy, Phys. Scr. **21**, 323 (1980).

[26] K. Andersson, P. Å. Malmqvist, B. O. Roos, A. J. Sadlej, and K. Wolinski, J. Phys. Chem. **94**, 5483 (1990).

[27] K. Andersson, P. Å. Malmqvist, and B. O. Roos, J. Chem. Phys. **96**, 1218 (1992).

[28] A. Zaitsevskii and J. P. Malrieu, Chem. Phys. Lett. **223**, 597 (1995).

[29] J. Finley, P. Å. Malmqvist, B. O. Roos, and L. Serrano-Andrés, Chem. Phys. Lett. **288**, 299 (1998).

[30] Z. Barandiarán and L. Seijo, Can. J. Chem. **70**, 409 (1992).

[31] R. D. Cowan and D. C. Griffin, J. Opt. Soc. Am. **66**, 1010 (1976).

[32] S. Huzinaga, L. Seijo, Z. Barandiarán, and M. Klobukowski, J. Chem. Phys. **86**, 2132 (1987).

[33] S. Huzinaga and A. A. Cantu, J. Chem. Phys. **55**, 5543 (1971).

[34] R. M. Pitzer and N. W. Winter, J. Phys. Chem. **92**, 3061 (1988).

[35] C. Teichteil, M. Pelissier, and F. Spiegelmann, Chem. Phys. **81**, 273 (1983).

[36] F. Rakowitz, M. Casarrubios, L. Seijo, and C. M. Marian, J. Chem. Phys. **108**, 7980 (1998).

[37] MOLCAS version 5, K. Andersson, M. Barysz, A. Bernhardsson *et al.*, Lund University, Sweden, 2000.

[38] COLUMBUS suite of programs. (ARGOS, CNVRT, SCFPQ, LSTRN, CGDBG, and CIDBG.) R. M. Pitzer (principal author). See: A. H. H. Chang and R. M. Pitzer, J. Am. Chem. Soc. **111**, 2500 (1989), and references therein for a description. CNVRT and LSTRN have been adapted to handle AIMP integrals by L. Seijo. CIDBG has been modified for spin-free-state-shifted spin–orbit CI calculations by M. Casarrubios.

[39] L. Seijo, Z. Barandiarán, and B. Ordejón, Mol. Phys. **101**, 73 (2003).

[40] L. Seijo, Z. Barandiarán, and E. Harguindey, J. Chem. Phys. **114**, 118 (2001).

[41] T. H. Dunning and P. J. Hay, in *Modern Theoretical Chemistry*, edited by H. F. Schaefer, III (Plenum, New York, 1977).

[42] *Gaussian Basis Sets for Molecular Calculations*, edited by S. Huzinaga (Elsevier, Amsterdam, 1984).

[43] A. Al-Abdalla, Z. Barandiarán, L. Seijo, and R. Lindh, J. Chem. Phys. **108**, 2005 (1998).

[44] C. Reber, H. U. Güdel, G. Meyer, T. Schleid, and C. A. Daul, Inorg. Chem. **28**, 3249 (1989).

[45] M. Casarrubios and L. Seijo, J. Mol. Struct.: THEOCHEM **426**, 59 (1998).

[46] S. Sugano, Y. Tanabe, and H. Kamimura, *Multiplets of Transition-Metal Ions in Crystal* (Academic, New York, 1970).

[47] Z. Barandiarán and L. Seijo (unpublished).

[48] C. A. Morrison, J. Chem. Phys. **72**, 1001 (1980).

[49] M. Bettinelli and R. Moncorgé, J. Lumin. **92**, 287 (2001).

[50] E. J. Heller, J. Chem. Phys. **62**, 1544 (1975).

[51] E. J. Heller, Acc. Chem. Res. **14**, 368 (1981).

[52] J. I. Zink and K. S. Shin, *Advances in Photochemistry* (Wiley, New York, 1991), Vol. 16, pp. 119–214.